



Study on Sol–Gel Synthesized IN800 Thermal Barrier Coatings Subjected to Thermal Cyclic Loading: Effect of Metallic Substrates

Dipak Kumar¹ · K. N. Pandey²

Received: 26 March 2020 / Accepted: 16 July 2020 / Published online: 12 August 2020
© The Korean Institute of Metals and Materials 2020

Abstract

In this work, the effect of sol–gel deposited top-coat on thermal fatigue resistance of thermal barrier coatings (TBCs) subjected to thermal fatigue loading is evaluated experimentally. To obtain non-conventional sol–gel thermal barrier coatings (SGTBC), coated samples underwent thermal fatigue loading at 1100 °C for 10 min heating and cooling. The tested sol–gel thermal barrier coatings were then compared to conventional air plasma sprayed (APS) thermal barrier coatings as well. The life of samples was investigated as a function of number of sustaining thermal cycles to times. Furthermore, the performed experiment was analyzed using scanning electron microscope, energy dispersive spectroscopy and X-ray diffractometer. The obtained results indicated that the non-conventional sol–gel thermal barrier coatings exhibited 1.46 times better thermal fatigue life in IN800SGTBC against 1.31 times thermal fatigue life of IN718SGTBC but overall thermal fatigue life was found to be better in IN718 SGTBC, signified effects of metallic substrates in thermal fatigue life determination. However, the nanostructured SGTBC had higher thermal cyclic resistance than conventional APS TBC, resulted in improved lifetime indicating the increased adherence at the substrate interface. Results also showed that the dominant failure mechanism of TBCs was destabilization of top-coat (YSZ), resulting composition of (Al, Cr)₂O₃ and spinel as reaction products for depleting Y₂O₃ producing from yttria stabilized zirconia (YSZ). Furthermore, the results showed that the amount of the porosity percent in the sol–gel TBCs was 2.3% higher than the conventional TBCs.

Keywords Inconel 800 · Air plasma spraying · Sol–gel effect · Microstructure characterization

1 Introduction

As it is very well known that IN800 superalloys are high temperature materials. With the increase calling for the engine performance, inlet temperature of the working fluid is also needed to increase. But superalloys have limitation of withstanding temperature of the working fluid which can be improved by coating the blade by ceramic material [1–4]. Hence, the ceramic coating was chosen as a shield against the harsh environment of high temperature [5–8]. These ceramic coatings are called thermal barrier coatings (TBCs). Typically, TBCs are duplex deposited systems; bond coat (BC) and yttria-stabilized-zirconia (YSZ) based

top-coat (TC). TBCs are classically constructed by two methods; Electron Beam–Physical Vapor Deposition (EB-PVD), (for turbine blades), or Air Plasma Spraying (APS), (for combustion chambers) [9–11]. EB-PVD coatings provide columnar microstructure which accommodates lateral thermo-mechanical stresses and strains due to the existence of elongated grains and laterally developed grain boundaries. Due to these reasons, porosities are produced in columnar way and these columnar porosities is the main reason for not having the good thermal conductivity of EB-PVD coatings between the exterior surface of the coating and the superalloy substrate [1–4]. Comparatively, APS produces twice lower thermal conductivity, 0.7–0.9 W m⁻¹ K⁻¹ except the case of accommodation of lateral thermo-mechanical stresses [12–14]. In spite of these few limitations, there are several advantages of APS techniques in terms of lower application cost, high deposition efficiency and coating ability to larger variety of components with a wider composition range [15–17]. Traditionally, 7 wt% yttria stabilized zirconia (7YSZ) is used for top coat in TBCs [18, 19] but it is suitable

✉ Dipak Kumar
dipakmnnit@gmail.com

¹ Mechanical Engineering Department, RKGIT, Ghaziabad, U.P. 201003, India

² Mechanical Engineering Department, Motilal Nehru National Institute of Technology, Allahabad 211004, India

for the temperature less than 1250 °C for enduring applications. For higher temperature, phase stability and porosity of YSZ coating systems is disturbed by the formation of cracks, resulting the increasing the chance of TBCs failures with the rise in thermal conductivity [20, 21]. Henceforth, for next generation turbine engines, which require ultra-high temperature capability, low thermal conductivity and durability, novel ceramic materials such as $\text{La}_2\text{O}_3\text{-Y}_2\text{O}_3\text{-ZrO}_2$, $\text{Gd}_2\text{O}_3\text{-Y}_2\text{O}_3\text{-ZrO}_2$, $\text{La}_2\text{Zr}_2\text{O}_7$, $\text{La}_2\text{Ce}_2\text{O}_7$, $\text{LaMgAl}_{11}\text{O}_{19}$ may be alternate or alternate coating techniques can be employed [22]. In the alternate of above mentioned reported novel TBCs, another alternate TBCs is nano-structured zirconia based TBCs. The nano-structured TBC could be made via sol–gel chemical route. It has found that this coating has high bonding strength [23], low thermal conductivity [24, 25] and robustness against thermal loading or cycling loadings [26–31].

Processing of sol–gel based dip-coating, chemical route deposition of either thin or thick TBCs shows non-oriented microstructures by the random pore network [32]. Sol–gel based deposition has multi-purpose advantages such as good homogeneity, simple and economical process, low sintering temperature and ease of application on complex geometry. Viazzii et al. [14] used sol–gel synthesized YSZ materials to coat on NiCrAlY bond-coat/Hastelloy-X. In this direction, Pin et al. tested and reported improvement in sol–gel based TBCs life at 1100 °C and 1150 °C. For this, they were used two different sol–gel methods namely dip-coating and spray-coating [33–35]. Viazzei et al. [14] were worked on chemical interface between NiCrAlY bond coat and Hastelloy-X for depositing the successfully the top-coat of YSZ. Further, Pin et al. [36] developed Thermal barrier coatings (TBCs) onto NiPtAl bond coated AM1 superalloy substrates by means of the dip-coating technique comprising in the immersion of the substrate into the slurry on a withdrawal rate of 250 mm per min to uniformly shape the coatings. Typically, they obtained the coatings thickness in the ranging of 50–150 μm . Furthermore, they worked for improving the diffusion barrier effect by bond coat, deposited on metallic substrate, pre-oxidation approaches. Along with this, developing of crack network induced from sintering heat treatment with

subsequently controlling of crack network by reinforcement of the TBC with a partially filling those cracks using sol–gel spray-coating were reported [36]. In this areas, Hajizadeh-Oghaz et al. [37] extensively worked on synthesis and characterization for TBC applications.

Up to now, no one is reported on Inconel series of superalloys, especially IN800 superalloys. More certain thick sol–gel coating thickness were optimized and obtained. For thermal fatigue testing on sol–gel thermal barrier coatings (SGTBCs), conventional test set-up, thermal cyclic furnace (TCF), and cyclic loading parameter is adopted, which is being used on conventional TBCs. Success of techniques depends their versatility. For this, thermal fatigue testing results were compared with IN718 superalloys for knowing the effects of metallic substrates. To explore the more possible use in the alternate of conventional APS TBC, SGTBC were compared with APS TBCs. Furthermore, fractography analysis is done using on scanning electron microscopy (SEM) coupled with elementary dispersive spectroscopy (EDS) and X-ray diffractometer (XRD).

2 Experiment

2.1 Conventional APS Dry Route 7YSZ TBC Deposition

For present study, Inconel 800 substrates were taken and their composition is shown in Table 1. Substrates were prepared, before coating as per protocol [38]. A $150 \pm 30 \mu\text{m}$ thicknesses of CoNiCrAlY, AMDRY9951, was deposited on the prepared substrate by Air Plasma Spraying (APS), F4-MB plasma gun (Sulzer Metco, Wolhen, Switzerland). Over to bond coat, the top-coats; 7 wt% yttria-stabilized zirconia (7YSZ) powder (Chemical composition as per AMPERIT No. 827-054, make H.C. Stark, Germany) were applied in the case of conventional TBCs. For deposition parameters for bond-coat can be seen in Table 2 and for top-coat it is referred in Table 3 [39, 40]. Figure 1 refers to the anatomy of a TBC system and Fig. 2 refers to the structure of conventional feedstock that were used in the present studies.

Table 1 Chemical composition (wt%) of Inconel 800

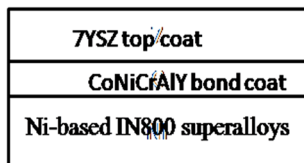
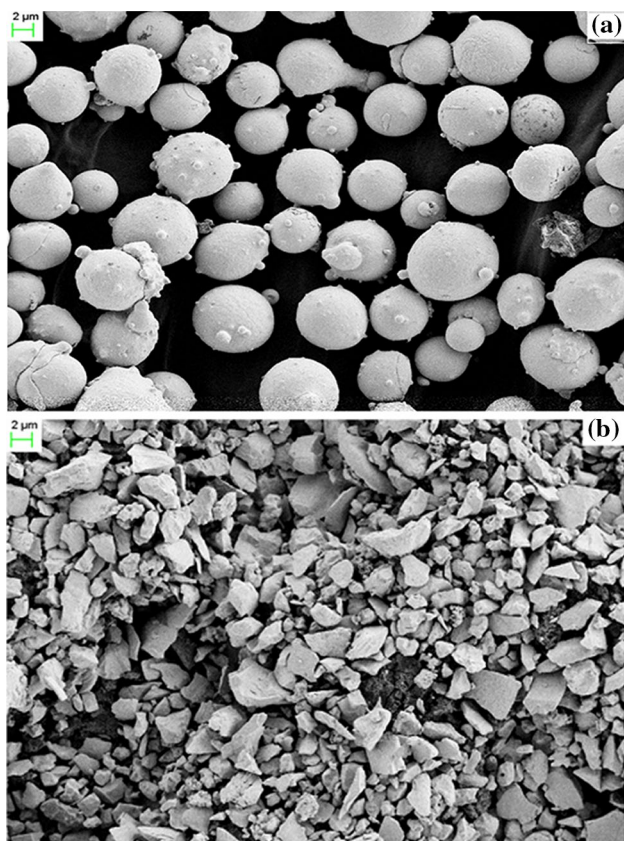
C	Si	Mn	S	P	Cr	Mo	Co	Fe	Ni
0.078	0.39	0.641	0.012	0.021	19.966	0.086	0.036	32.407	Balance

Table 2 Spraying process parameters for bond coat CoNiCrAlY

Current (A)	Voltage (V)	Primary gas (Ar) (l/min)	Secondary gas (H ₂) (l/min)	Powder feed rate (g/min)	Spray distance (mm)	Travel speed (mm/s)
550	67	43	9.5	20	102	30

Table 3 Optimized air plasma spraying process parameters for 7YSZ top coat

Current (A)	Voltage (V)	Primary gas, Ar (l/min)	Secondary gas, H ₂ (l/min)	Powder feed rate (g/min)	Spray distance (mm)	Travel speed (mm/s)
550	75	60	6	30	100	30

**Fig. 1** Anatomy of a square-shaped TBC system**Fig. 2** Surface morphology of thermal sprayed feedstock: (a) CoNiCrAlY powder, (b) conventional 7YSZ powder

2.2 Un-Conventional Sol–Gel Chemical Route YSZ TBC Deposition by Cyclic Dip Coating

During this process, superalloy IN800 substrates were initially bond coated with CoNiCrAlY to improve TBC adhesion. To fabrication of top-coat by sol–gel route, 7YSZ sol were made from zirconium (IV) propoxide [Zr(OPr)₄] (M/s Sigma Aldrich) and yttrium (III) nitrate hexahydrate

(M/s Across Organics) [41]. In this process, Acetyl acetone (AcAc) was used as complexing agent. The complexation ratios and hydrolysis ratios as optimized sol–gel process parameters were taken as 0.9 and 10.5 respectively [14, 33]. Superalloy substrates were dipped and withdrawn into the composite sol–gel at a controlled rate of 250 mm/min for the coatings. The cyclic dip coating parameter was 20-min heating at 65 °C dry temperature and 10-min dipping until the achieving required TBC thickness. Finally, optimized 120 μm thickness of TBC were obtained under the optimized heat treatment conditions of 900 °C temperature for 3 h.

2.3 Thermal Cyclic Testing

In thermal cyclic testing, each cycle consisting of heating, dwelling at elevated temperature, cooling and dwelling at the minimum temperature. Heating rate and cooling rate was taken as 110 °C/min and 10 °C/min, respectively. Schematic set up for thermal cyclic fatigue test is shown in Fig. 3, and their testing program can be shown in Fig. 4.

Analysis of failure of TBC systems was done by measuring the weight of the TBC sample on an electronic balance weighing machine after every 10 cycles. During the experiments no percentage of spallation criteria were adopted because of not getting any observable spallation percentage before 100% spallation of coatings.

2.4 TBC Characterization

The coating microstructure was characterized by Scanning Electron Microscope (SEM-FEG) equipped with EDS Field Emission Gun (FEG). Porosity percent of TBC was determined using Matlab from SEM-FEG micrographs of TBC.

3 Results and Discussion

3.1 Microstructure of Sol–Gel Dip Coated and Plasma Sprayed Conventional Coatings

Figure 5a, b presents the cross-section image of dip-coated TBCs and plasma sprayed TBCs whereas Fig. 5c indicating the sol–gel synthesized dip coated TBCs as a proof, which approves the thermal fatigue testing was performed on nine number of samples. For convenience only, sol–gel derived TBCs sample is presented in Fig. 5c. However, same number

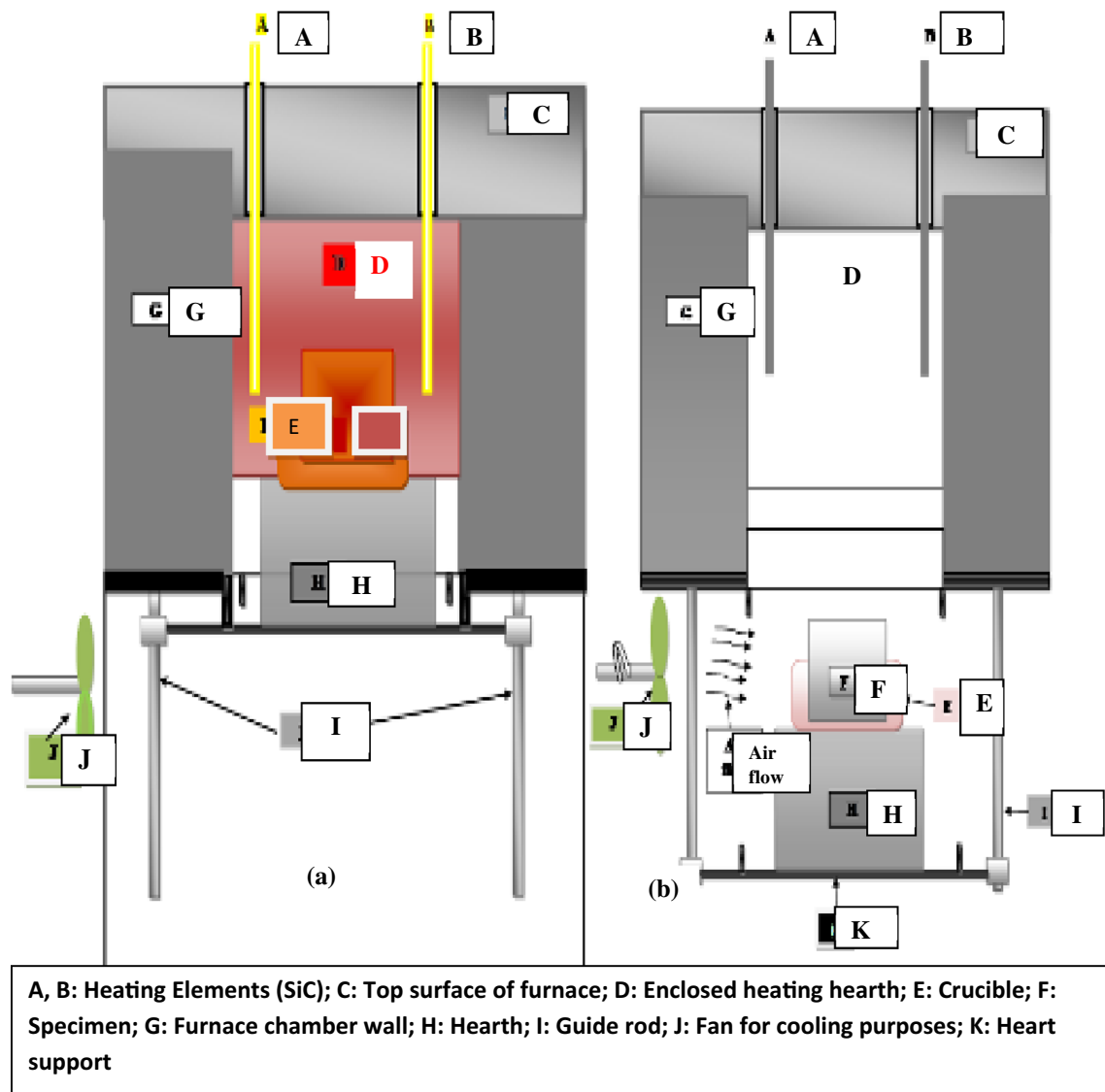


Fig. 3 Schematic diagram of: (a) heating period, (b) cooling period

of samples was also taken for plasma sprayed TBCs subjected to thermal fatigue loading for obtaining the average thermal fatigue life of TBCs. Figure 6a, b address the surface topography of sol–gel dip coated TBCs. Figure 6a refers to the induced cracks during drying and heat treatment of sol–gel deposited TBCs. Cracks running through the surface generated due to drying stresses. Images were taken at different magnifications in various parts of the coated samples in order to have representative images of the surface topography. Dense cracking, as shown in Fig. 6a, produces the evidence of thick sol–gel thermal barrier coating. Figure 6b is enlarged view of Fig. 6a which shows three kinds of structures. First two are molted zone and unmelted zone, and the third one is partially molted zone. It also presents

homogeneity of coating layers. Figure 6c shows nano particle size of the coated surface, appearing bimodal structure as earlier reported in Ref. [23]. The bimodal structure is appeared all around the substrate surface which appears as “worm-like” grain morphology with a definite shape and size [42]. The higher magnification micrograph (Fig. 6c) shows no cracks or pores. The coated particles are of quasi-spherical shape, Fig. 6c. Elemental analysis of Fig. 6c shows that there is low concentration of yttrium as dopant in zirconium solvent.

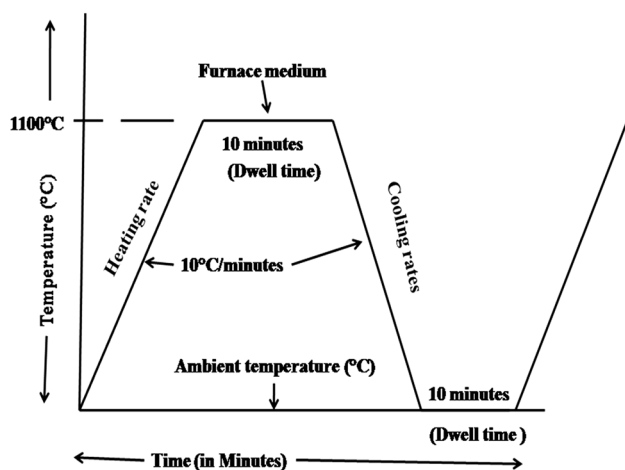


Fig. 4 Schematic diagram of time–temperature evolution cycles

3.2 Thermal Fatigue Behaviors of Unconventional and Conventional Plasma TBCs

The thermal fatigue behavior of sol–gel dip coated TBCs, where cracking and subsequent spallation is progressive as cracks first come together to finally demarcate individual YSZ coatings prone to local delamination [33, 34] in coating surface. Figure 7 refers scanning electron micrograph of IN800 SGTBCs after 423 life cycles. Different modes of fatigue failure of non-conventional thermal barrier coatings are shown in Fig. 7a. Big white circle is showing spalled top coat materials. The small white circle is representing the crack network. A different of cracks, viz. Vertical, horizontal and their mud can be observed (shown by white arrow) on within TBC or coat boundary section. Some chipping is also visible in Fig. 7a. Some of the coating layers is also damaged in the form of powder which is revealed in red arrows and, some parts of coating layers are damaged in Intra-granular spallation modes, which is shown in the red circular region of Fig. 7a. Figure 7b illustrates the cracks within TBC layers whereas some parts of coating layers can be seen in “debris” mode in the white circular region. Backscattered micrograph of superni 800 SGTBC after 423 cycles of thermal fatigue load is shown in Fig. 7c. Numbers of cracks are also visible within the top coat layer. White circular zone shows the completely damaged zone of the top coat layers. Zirconium associated yttrium with high spectrum presents the top coat layers as YSZ is also adherent to bond coat. The CoNiCrAlY bond coat layer below the top coat layer of Y-Zr element shows the spinel oxide formation during thermal fatigue testing. This spinel oxide results in crack formation before spallation of the coating layer.

In the case of dip coating, the coating surface prior to thermal fatigue is quite different as cracks are clearly observed, Figs. 6a, b and 7. For the dip-coating TBC,

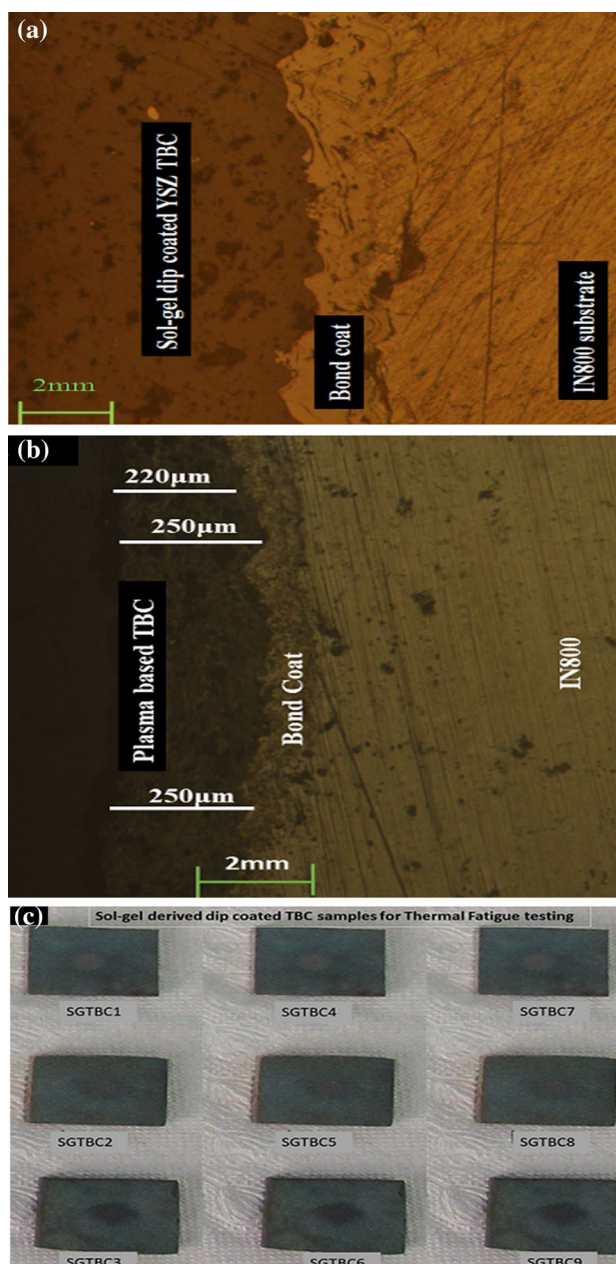


Fig. 5 Optical micrograph of polished cross section of: (a) Sol-gel dip coated 7YSZ TBC, and (b) Plasma sprayed TBC; and (c) Sol-gel synthesized Dip-coated TBC sample

thermal fatigue damage takes place through the pre-existing initial crack network (Fig. 6a) by widening of the cracks within the top coat layers or along the TC/BC interface. In Fig. 7c, oxygen appears on one of the peaks of spectra showing the oxide formation of the respective element. Aluminum is also appearing on the peaks of spectra showing the depletion of thermally grown oxide (TGO) layer due to spinel oxide formation [43, 44], turns out to be in rapid and extended surface damage crack combination, enlargement

Fig. 6 SEM micrograph of dip coated SG-YSZ thermal barrier coatings (a, b) two different magnification and c nano zone coating structure with very high magnification showing nano size structure

and propagation. The crack propagation reversed back on the coating surfaces, resulting in spallation of the coating layer.

Figure 8 shows the scanning electron micrograph of conventionally IN800TBC after 290 life cycles, which illustrates white and black fractures zones. In Fig. 8a, unfractured spherical splates are observed within the circular zone while white fractures present the top coat layers, see in. Figure 8b, in the form of debris on high magnification. Figure 8c presents the backscattered electron micrograph of failed plasma TBC after 290 thermal cycles. Figure 9 presents the EDS analysis of different damaged zones of APS coated sample after 290 cycles of thermal fatigue load. Figure 8c refers to zonal spectrum for elemental analysis. Analysis of spectrum 1 as shown in Fig. 9a, which is for selected area 1 of Fig. 8c, reveals that along this area of the coating the dominant spectrum is for Y and Z. Therefore, the top coat is not damaged in this area. Spectrum 2 (Fig. 9b) which is for area 2 of Fig. 8c composed of dominant Cr and alumina. So spectrum 3 (Fig. 9c) is for area 3 of Fig. 8c and it consists of dominant Cr and Al which indicates adherence of the top coat layer to thermally grown oxide (TGO) layer, which indicates that the fracture has taken place in the interface of TGO/TC leaving the TGO intact except the large bulk oxides of Cr_2O_7 . Spectrum 4 (Fig. 9d) is EDS for area 4 of Fig. 8c and it consists of a dominant pure alumina layer followed by chrome layer. Spectrum 5 shown in Fig. 9, which is EDS of area 5 as shown in Fig. 8c, presents the spinel oxide (mixed oxides of Ni, Cr and Co). Analysis of these spectrums reveals that in some cases, fracture happened along BC/TGO interface (Spectrum 2, 4, and 5). Figure 8b, c show that the fracture occurred entirely on the TGO/TC interface and thin alumina TGO layer was intact (Spectrum 2, 3, and 4). Along some area of the specimen interface of TC/TGO and TGO/TC were also fractured. For more detail, EDS analysis were done which shows a large area of TGO covering as a thin layer of alumina on top of some colonies having the composition of $(\text{Al}, \text{Cr})_2\text{O}_3$ and spinels. From the EDS elemental analysis, it is observed that the interface TGO is either damaged or cracked, Fig. 8. This interface TGO cracking is possible reason of shifting from white fracture to mixed fracture. This mixed fracture was also confirmed by spectrum 1, 2, 3, 4, as shown in Fig. 9. The formation of mixed–element oxide, exhibiting composition of bond coat, is also observed to be affected adhesion bonding between BC and TC subjected to thermal cyclic loadings. The phenomenon responsible for this is likely to be clustering of mixed oxide, Fig. 9. A similar phenomenon was observed by various researcher, viz. Eriksson et al. [45],

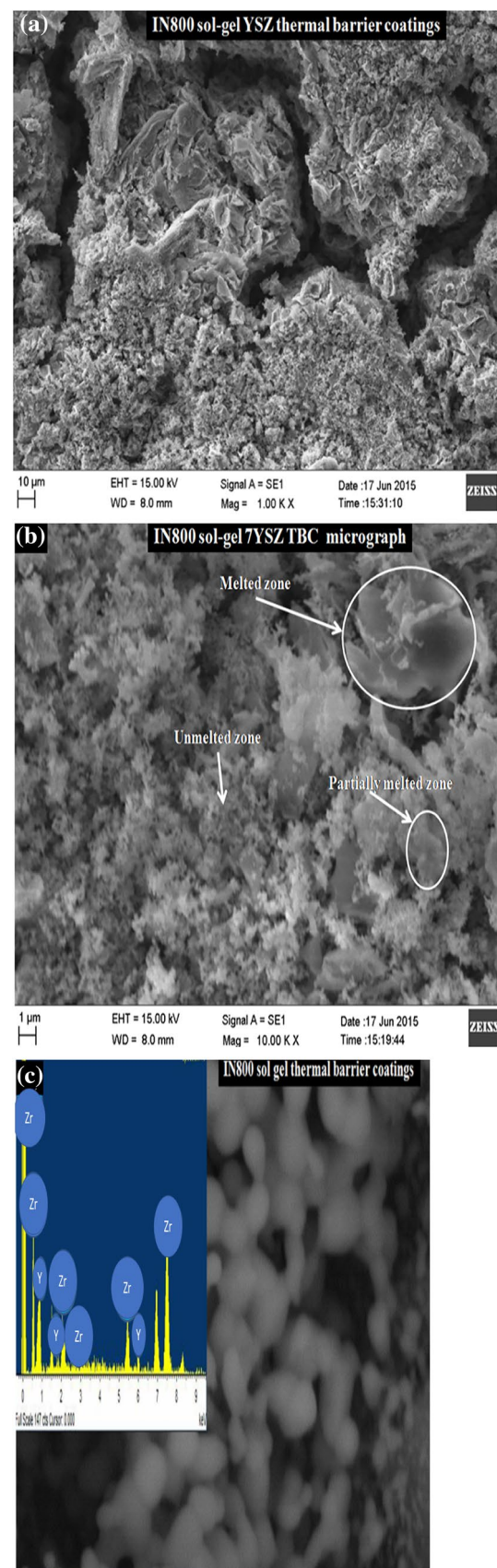


Fig. 7 SEM micrograph of IN800 SG TBC after 423 thermal fatigue life (a & b) at two different magnifications, and (c) back scattered image

Chen et al. [46] and Nesbitt et al. [47] and was also reported that this clustering phenomenon may behave as source of crack nucleation sites, initiation, propagation and ultimately damaging of oxide clusters.

Cracks which grows in the coating may be interlamellar and translamellar. Cracks which grow between the layers of splates, breaking the bond between the splates is called interlamellar, Fig. 7c. Translamellar crack grows by breaking the splates itself, Fig. 7c. Sol–gel based TBC on IN 800 fails under thermal fatigue as white fracture, as shown in Fig. 7c, where as conventional APS TBC shows white fracture and black fracture both, Fig. 8b, c. Other types of fracture are also visible, such as translamellar (through-splat) fracture, shown in Figs. 7 and 8.

3.3 Thermal Fatigue Lifetime

Figure 10 shows the macroscopic images of the sol–gel dip coated nanostructured TBCs and conventional air plasma spray TBCs during thermal cyclic testing. In the case of both coatings, thermal fatigue was observed starting from either the edge or the corners of the square samples, independent of shape, followed by propagation to the adjacent areas. It clears that sensitiveness of edges or corners towards extreme heating and cooling, resulted in thermal stresses at the edges/corners. The induced set-up thermal stresses may be caused of failure in TBCs [30, 31, 48, 49]. Similar study but with Inconel718superalloys substrates [50] was earlier reported. In both Fig. 10a, b, the spalled regions of top coat surface for both conventional and unconventional coatings are indicated by white arrows. Difference of failure in sol–gel derived TBCs and conventional TBCs is easily observed from Fig. 10. Figure 10a shows the failure of TBCs at TC/BC interface and whereas Fig. 10b shows the failure of TBCs at TC/TGO interface. In most of the top coat materials, YSZ is intact as shown in Fig. 10a. It was also confirmed by EDS analysis (Fig. 7c). Intacting of top coat materials to the bond coat after thermal fatigue indicates the good chemical bonding to bond coat materials against thermal cyclic loadings at 1100 °C. In Fig. 10b, left side shows the spalled top coated materials and right side shows the failed plasma TBC specimens. In Fig. 10b, black spots indicate the mixed oxide formation before spallation which was also confirmed by EDS analysis in Fig. 9 [50].

Figure 11 elucidates the coating failure in terms of weight change as a function of number of thermal cycles for both nano-structured sol–gel TBCs and conventional TBCs. Figure 11a test also exhibited excellent thermal cyclic

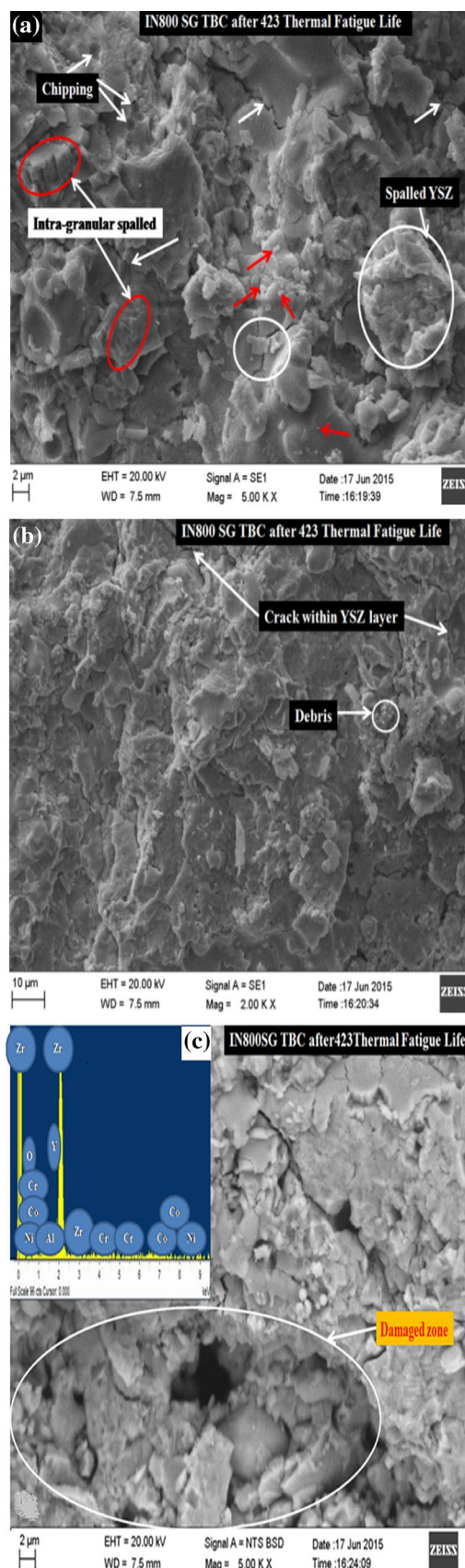


Fig. 8 SEM micrograph of IN800 plasma TBC after 290 thermal fatigue life (a & b) at two different magnifications (c) back scattered electron image

performance of sol–gel TBCs in comparison to conventional TBCs during thermal fatigue testing. In the case of unconventional TBCs, weight of the sample initially decreased due to sintering effect and then remained almost constant for remaining life before a sudden drop in weight with increase in number of thermal cycles. After 125 thermal cycles, a weight loss was observed that could be due to start of spallation from edges. Weight again remains constant till 332 thermal cycles. After 332 cycles, again some weight loss was repeatedly observed in each sample testing, may be indication of spallation. After 423 cycles, there some sudden weight drops observed, implying that coating spallation was significantly occurred, indicating sol–gel TBCs failures. In the case of conventional coating, Fig. 11b, initially gain of weight was observed due to coating material oxidation and then weight loss after some cycles. Weight of the sample was almost constant up to 290 thermal cycles. After 290 cycles, there was a sudden weight drop observed which elucidated complete failure of the coating. Before 290 numbers of cycles, there was a small drop in weight, which is due to start of spallation from the edges of the sample. The thermal cycle curve shown in Fig. 11a shows a stepwise weight loss in comparison to thermal cyclic curve shown in Fig. 11b for conventional coating. This is due to multilocational damage in sol–gel TBCs in comparison to conventional TBCs [50]. However, comparatively better thermal fatigue life was observed if IN718 superalloys substrates were used in the place of IN800 superalloys substrate, can be seen in the Fig. 11c, d.

The thermal fatigue life of the conventional and unconventional TBCs are explicitly presented in Fig. 12. It can be elucidated that the unconventional IN800TBCs shows 1.46 times superior life in comparison to the conventional TBCs. Similar results are also reported by other researchers [48]. Growing sol–gel TBC life, as compared to the plasma TBC, can be described concerning coating microstructures [50]. Enhanced strain tolerance of sol–gel TBCs against thermal fatigue loadings at 1100 °C was thinkable due to in-built porosities and micro-cracks in sol–gel TBCs, Fig. 5a. The porosities as well as micro-cracks decrease both elastic modulus and thermal stresses and hence stress relaxation takes place [51–58]. Advantages of coating degradation in each stage attributes to control the crack propagation rate in SG TBCs. Same type of phenomenon in the thermally–sprayed nano-structured TBCs is also reported by other authors [50, 59–61]. Other reason of improved thermal cycles in sol–gel derived TBCs might be due to arresting and deflecting of crack propagating through splat-boundaries after striking the

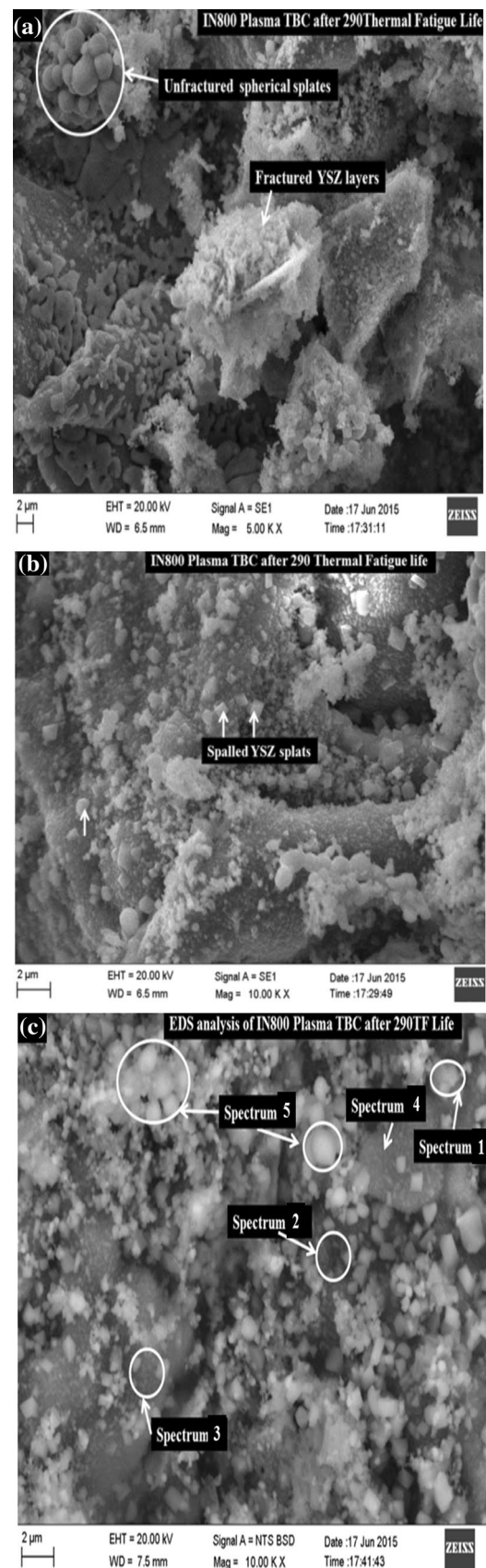
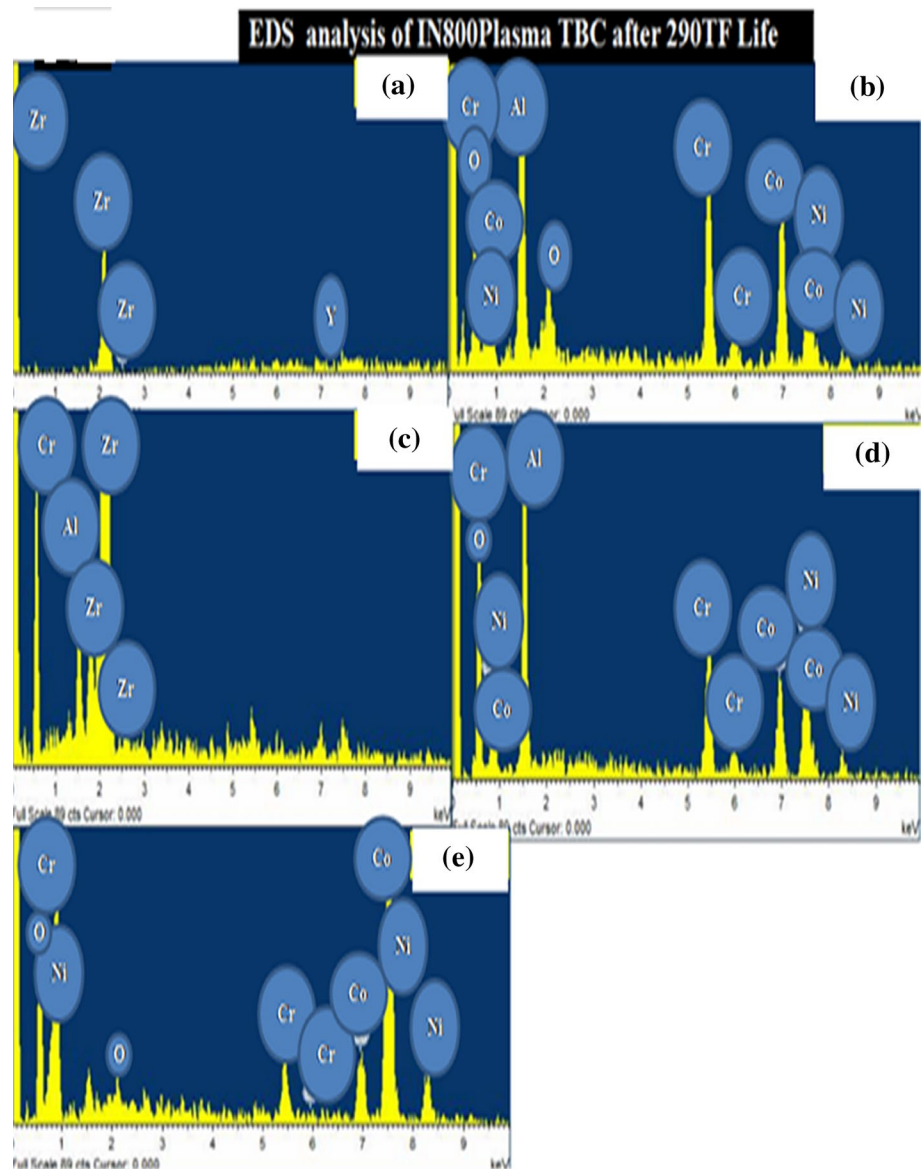


Fig. 9 a–e EDS analysis of IN800 plasma TBC after 290 thermal fatigue life at five different 1–5 locations corresponding to spectrum 1–5 in figure 8c

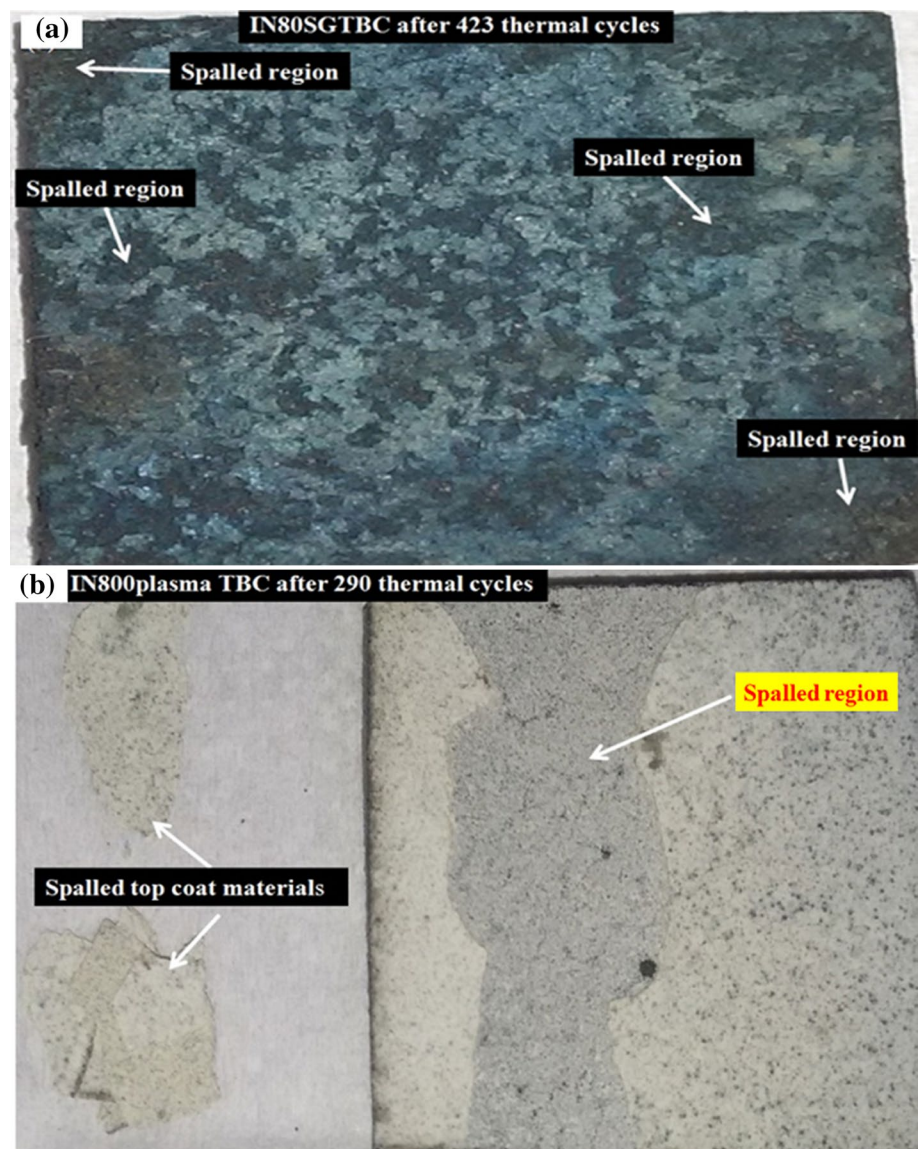


crack/s with the nano-particles. This step-down laddering nature of thermal cycles was observed as long sustainability against high thermal cyclic loadings in comparison to APS TBCs. Due to arresting and/or deflection of crack from its original path, it takes time to propagate parallel to TC/BC interface to cross the width of coating layers. Once the crack crosses the width of an YSZ top-coat layer, the barrier loses its chemical bonding to bond coat, hence separated in individual spall. This process continues as the thermal cyclic loading progresses till the failure of coatings [50].

Comparative XRD patterns of conventional air plasma sprayed 7YSZ TBCs and sol–gel YSZ TBCs are shown in Fig. 13. Figure 13a, which is XRD pattern of conventional APS 7YSZ, shows the non-transformable tetragonal (t-phase) phase. Although, after prolong thermal cycling, Metastable non-transformable tetragonal phase was found

which was occurred due to possible diffusion of yttria and transformation probability from tetragonal to monoclinic since ZrO_2 is martensitic in nature. This transformation reason affects the coating structural integrity [49, 62–65]. However, no phase transformation was observed during the thermal fatigue of 7YSZ conventional coatings in the present study (Fig. 13a). For the case of as-derived sol–gel 7YSZ TBC, tetragonality phase was also observed in Fig. 13b. It was also confirmed by JCPDS Data Nos. (01-080-2187, 01-078-3348) as peak No. 1 and peak No. 5; JCPDS Data Nos. (01-070-4433; 01-070-4430) as peak No. 4; JCPDS Data No. (01-070-4426) as peak No. 6. Peak No. 2 shows the presence of YSZ but it is in transformation phase may be due to presence of Y_2O_3 . The Y_2O_3 comes from $Y(NO_3)_3 \cdot 6H_2O$ which was added in parent chemical $Zr[(PrO_4)]_4$ during

Fig. 10 Photographs of (a) SG-YSZ IN800TBC (b) 7YSZIN800TBC samples after thermal fatigue testing



sol–gel synthesis. Presence of $Y(NO_3)_3 \cdot 6H_2O$ was also confirmed by JCPDS data No. (00-032-1435) as peak No. 3.

In Fig. 11b, the XRD data of thermal fatigue dip coated SGYSZ TBC is shown XRD data shows that thermal fatigue of this conventional coating has occurred due to either by the formation of Al–Ni mixed metallic oxide or spinel oxide. Peak No. 1 indicates the presence of Ni_3Al (JCPDS data No. 00-002-0416), peak 1' (JCPDS data No. 00-058-0564) as NiCoCr, peak 2 (JCPDS Data No. 03-065-8490, 01-073-8778) as spinel oxide, peak 3 (JCPDS data No. 00-020-0019) as Al–Ni elemental oxide formation. The reported XRD spectrum agrees with the EDS analysis reported in Fig. 9. In TBC systems, thermal stresses must likely to induced because deposited coating layers and underlying metallic substrates must possessed different coefficient of thermal expansion (CTE, α) under thermal cyclic loading

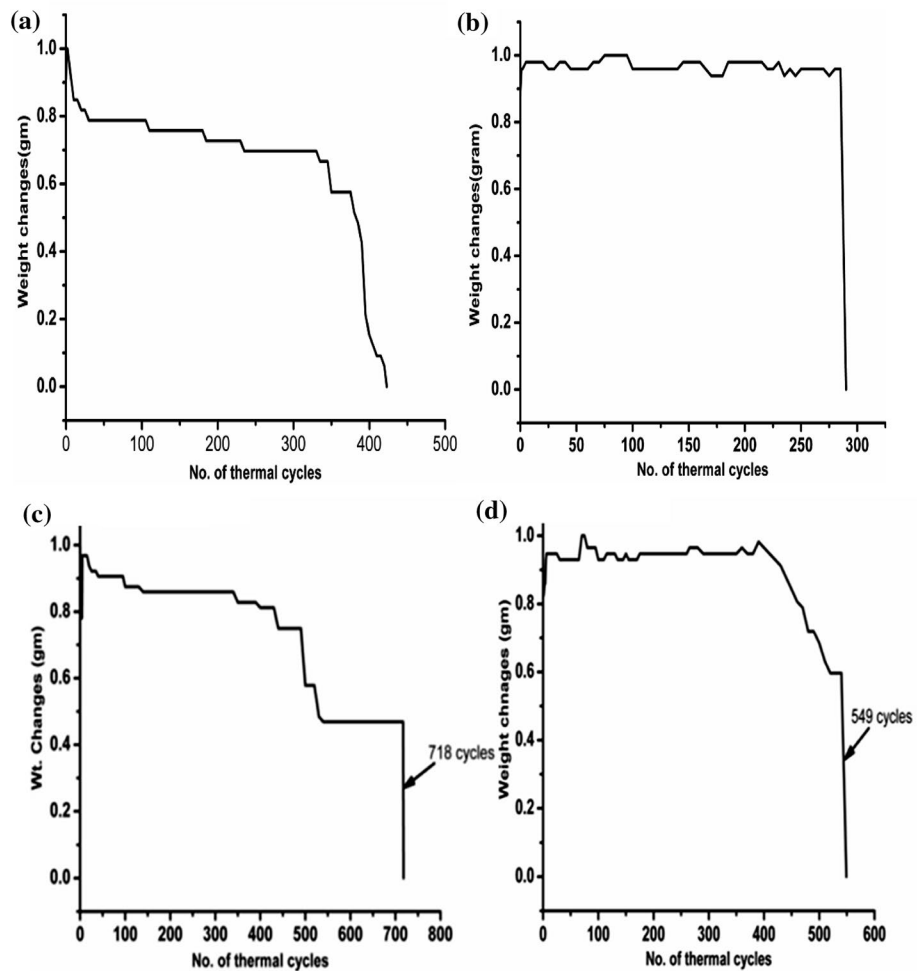
since all part of TBC systems behaves as different materials. Therefore, it can be said that CTE mismatch, one of the key factors, will be remain responsible reason for the failure of TBCs [57, 65].

To conclude this work, sol–gel synthesized thermal barrier coatings fabricated with YSZ ceramics are conceivable competitors to the conventional TBC systems. During sol–gel process before and after thermal cyclic testing it was also observed various rewards in views of process cost, and reproducibility. Similar observations were reported by other authors [66, 67].

3.4 Effect of Porosity on TBCs

At present, TBC manufactured by APS have a porosity of about $14 \pm 3\%$. But, percentage of porosity in SGTBCs is

Fig. 11 Weight changes as a function of cycle number for (a) IN800 SGYSZTBC, (b) IN800APS TBCs, (c) IN718 SGYSZTBC, (d) IN718APS TBCs, during thermal cyclic testing



$34.21 \pm 3\%$. So, the porosity of current SGTBC systems is comparatively investigated greater than that of conventional APSTBC systems which allows the sol-gel TBC obtaining better thermal cycling resistance than APSTBC systems.

4 Conclusion

The objective of the current paper was to examine the microstructure and capability of the sol-gel chemistry, which were established by dip coating method, between CoNiCrAlY coating and IN800 superalloy against thermal cyclic loading on programmable thermal cyclic furnace and then it was compared with IN718 based SGTBC. The significant outcomes can be brief as follows:

- With the various properties possessed by deposited coating and underlying metallic substrates subjected to thermal cyclic loading induced thermal stresses were found foremost reason of TBC failures, i.e. independent of coating methodology.

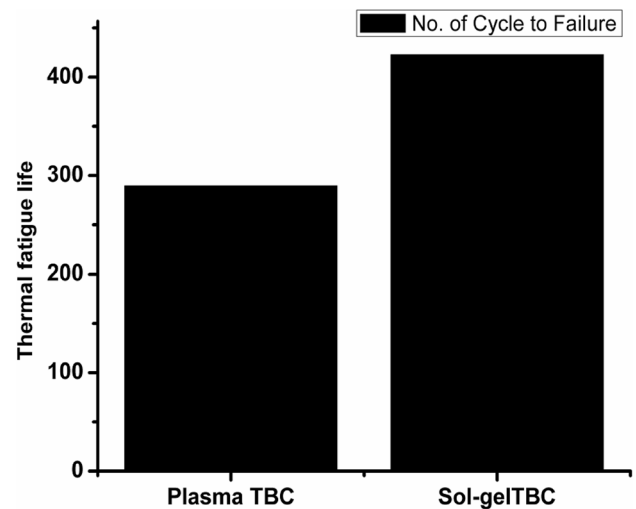


Fig. 12 Thermal cycling lifetime of the conventional and sol-gel TBCs

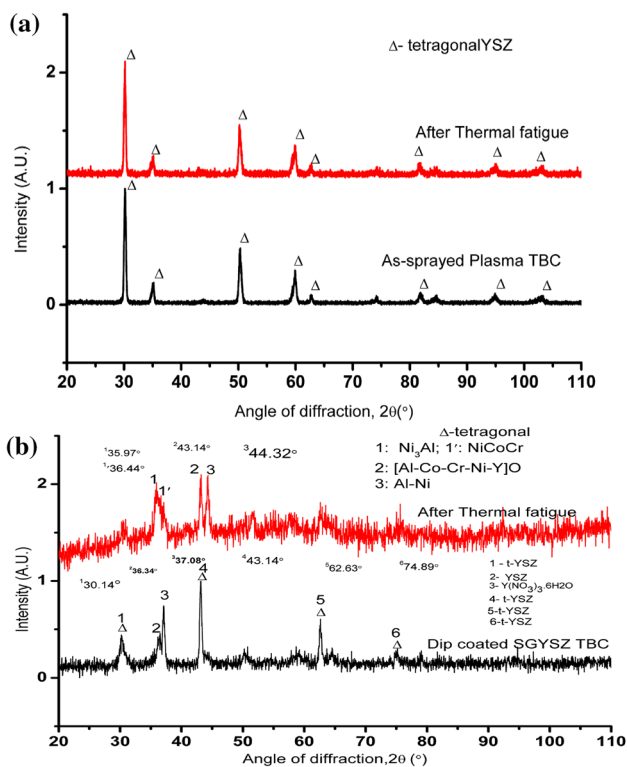


Fig. 13 Comparative XRD pattern of (a) conventional APS 7YSZ coatings and (b) sol-gel dip coated 7YSZ TBC before and after thermal fatigue testing

- 1.46 times better thermal fatigue life were obtained in IN800SGTBC against 1.31 times thermal fatigue life of IN718SGTBC but overall thermal fatigue life was found to be better in IN718 SGTBC, signified effects of metallic substrates in thermal fatigue life determination.
- Sintering might be another reason for the improvement of thermal cyclic resistance in sol-gel TBC specimens, which maintained a thin layer of TGO as clear from the EDS analysis.
- Weakening of Ytria Stabilized Zirconia (YSZ) were observed as a consequence of chemical reaction between the bond coat and sol-gel based top-coat due to the formation of some colonies having the composition of $(Al, Cr)_2O_3$ and spinel as reaction products, resulted in destructive phase transformation of YSZ from the tetragonal phase to the monoclinic one accompanied by volumetric expansion, clears from XRD results.
- Porosity percent in SGTBC was about 2.3% more than that of the porosity percent in the APS TBC.

References

1. J.R. Nicholls, K.J. Lawson, A. Johnstone, D.S. Rickerby, *Surf. Coat. Technol.* **151–152**, 383 (2002)
2. J. Fenech, M. Dalbin, A. Barnabe, J.P. Bonino, F. Ansart, *Powder Technol.* **208**, 480 (2011)
3. D.R. Clarke, S.R. Phillpot, *Mater. Today* **8**, 22 (2005)
4. X.Q. Cao, *J. Mater. Sci. Technol.* **23**, 15 (2007)
5. R.A. Miller, *J. Therm. Spray Technol.* **6**, 35 (1997)
6. C.T. Sims, *Adv. Mater. Process.* **139**, 32 (1991)
7. R. Vaben, S. Giesen, D.J. Stover, *J. Therm. Spray Technol.* **18**, 835 (2000)
8. B.H. Kear, E.R. Thompson, *Science* **208**, 847 (1980)
9. N.P. Padture, M. Gell, E.H. Jordan, *Science* **296**, 280 (2002)
10. A. Scrivani, G. Rizzi, U. Bardi, C. Giolli, M.M. Miranda, S. Ciattini, A. Fossati, F. Borgioli, *J. Therm. Spray Technol.* **16**, 816 (2007)
11. J.A. Haynes, M.K. Ferber, W.D. Porter, *J. Therm. Spray Technol.* **9**, 38 (2000)
12. X. Wang, W.H. Lan, P. Xiao, *Thin Solid Films* **494**, 263 (2006)
13. C. Ren, Y.D. He, D.R. Wang, *Surf. Coat. Technol.* **206**, 1461 (2011)
14. C. Viazzi, J.P. Bonino, F. Ansart, *Surf. Coat. Technol.* **201**, 3889 (2006)
15. S. Guo, Y. Kagawa, *Ceram. Int.* **33**, 373 (2007)
16. R. Rajendran, *Eng. Fail. Anal.* **26**, 355 (2012)
17. Y. Bai, Z.H. Han, H.Q. Li, C. Xu, Y.L. Xu, Z. Wang, C.H. Ding, J.F. Yang, *Appl. Surf. Sci.* **257**, 7210 (2011)
18. Z. Hong, L. Fei, H. Bo, W. Jun, S. Bao-de, *Trans. Nonferrous Met. Soc. China* **17**, 389 (2007)
19. L. Wang, Y. Wang, X.G. Sun, J.Q. He, Z.H. Pan, C.H. Wang, *Ceram. Int.* **38**, 3595 (2012)
20. P. Fauchais, G. Montavon, R.S. Lima, B.R. Marple, *J. Phys. D: Appl. Phys.* **44**, 53 (2011)
21. F. Davar, A. Hassankhani, M.R. Loghman-Estarki, *Ceram. Int.* **39**, 2933 (2013)
22. X.Y. Xie, H.B. Guo, S.K. Gong, *J. Therm. Spray Technol.* **19**, 1179 (2010)
23. H. Jamali, R. Mozafarinia, R.S. Razavi, R. Ahmadi-Pidani, M.R. Loghman-Estarki, *Curr. Nanosci.* **8**, 402 (2012)
24. R.S. Lima, B.R. Marple, *J. Therm. Spray Technol.* **17**, 846 (2008)
25. R.S. Lima, A. Kucuk, C.C. Berndt, *Mater. Sci. Eng. A* **313**, 75 (2001)
26. C. Zhou, Q. Zhang, Y. Li, *Surf. Coat. Technol.* **217**, 70 (2013)
27. D. Kumar, K.N. Pandey, *Int. J. Comput. Mater. Sci. Surf. Eng.* **6**, 75 (2015)
28. S.R. Choi, D. Zhu, R.A. Miller, *Int. J. Appl. Ceram. Technol.* **1**, 330 (2004)
29. C. Ramachandran, K.N. Lee, S.N. Tewari, *Surf. Coat. Technol.* **172**, 150 (2003)
30. R. Ahmadi-Pidani, R.S. Razavi, *Opt. Lasers Eng.* **50**, 780 (2012)
31. C. Giolli, A. Scrivani, G. Rizzi, F. Borgioli, G. Bolelli, L. Lusvardi, *J. Therm. Spray Technol.* **18**, 223 (2009)
32. C. Viazzi, R. Wellman, D. Oquab, J. Nicholls, D. Monceau, J.P. Bonino, F. Ansart, *Mater. Sci. Forum* **595–598**, 3 (2008)
33. L. Pin, F. Ansart, J.P. Bonino, Y.L. Maoult, V. Vidal, P. Lours, *J. Eur. Ceram. Soc.* **33**, 269 (2013)
34. J. Sniezewski, Y. LeMaoult, P. Lours, L. Pin, V.M. Bekale, D. Monceau, *Surf. Coat. Technol.* **205**, 1256 (2010)
35. L. Pin, F. Ansart, J.P. Bonino, Y.L. Maoult, V. Vidal, P. Lours, *Surf. Coat. Technol.* **206**, 1609 (2011)
36. L. Pin, V. Vidal, F. Blas, F. Ansart, S. Duluard, J.-P. Bonino, Y. Le Maoult, P. Lours, *J. Eur. Ceram. Soc.* **34**, 961 (2014)

37. M. Hajizadeh-Oghaz, R.S. Razavi, MdR Loghman-Estarki, J. Sol Gel Sci. Technol. **70**, 6 (2014)
38. D. Kumar, K.N. Pandey, D.K. Das, Int. J. Min. Metal. Mater. **23**, 934 (2016)
39. D. Kumar, K.N. Pandey, Proc. Inst. Mech. E Part L: J Mater. Des. Appl. **231**, 600 (2017)
40. D. Kumar, K.N. Pandey, D.K. Das, Proc. Inst. Mech. E Part L: J Mater. Des. Appl. **232**, 582 (2018)
41. D. Kumar, K.N. Pandey, Ind. J. Chem. Technol. **24**, 153 (2017)
42. M. Shane, M.L. Mecartney, J. Mater. Sci. **25**, 1537 (1990)
43. R. Ghasemi, Z. Valefi, Surf. Coat. Technol. **344**, 359 (2018)
44. R. Ghasemi, Z. Valefi, J. Alloys Compd. **732**, 470 (2018)
45. R. Eriksson, H. Brodin, S. Johansson, L. Ostergren, X. Hai, Surf. Coat. Technol. **243**, 82 (2014)
46. W.R. Chen, X. Wu, B.R. Marple, P.C. Patnaik, Surf. Coat. Technol. **201**, 1074 (2006)
47. J.A. Nesbitt, D. Zhu, R. Miller, C. Barrett, Mat. High Temp. **20**, 507 (2003)
48. H. Jamali, R. Mozafarinia, R.S. Razavi, R. Ahmadi-Pidani, Ceram. Int. **38**, 6705 (2012)
49. H. Jamali, R. Mozafarinia, R.S. Razavi, R. Ahmadi-Pidani, Ceram. Int. **38**, 6712 (2012)
50. D. Kumar, Trans. Indian Inst. Met. **72**, 1927 (2019)
51. R.S. Lima, B.R. Marple, Mater. Sci. Eng. A **485**, 182 (2008)
52. S. Bose, *Elsevier Science and Technology Books* (Connecticut, New York, 2007)
53. X. Cao, R. Vassen, D. Stoever, J. Eur. Ceram. Soc. **24**, 1 (2004)
54. R. Vaben, G. Kerkhoff, D. Stover, Mater. Sci. Eng. A **303**, 100 (2001)
55. Y. Liu, C. Persson, S. Melin, J. Wigren, J. Therm. Spray Technol. **14**, 258 (2005)
56. R. Vaben, F. Traeger, D. Stover, J. Therm. Spray Technol. **13**, 396 (2004)
57. H. Chen, X. Zhou, C. Ding, J. Eur. Ceram. Soc. **23**, 1449 (2003)
58. R.S. Lima, B.R. Marple, J. Therm. Spray Technol. **16**, 40 (2007)
59. M. Gell, E.H. Jordan, Y.H. Sohn, D. Goberman, L. Shaw, T.D. Xiao, Surf. Coat. Technol. **146–147**, 48 (2001)
60. R.S. Lima, B.R. Marple, Mater. Sci. Eng. A **395**, 269 (2005)
61. A.N. Khan, J. Lu, Surf. Coat. Technol. **201**, 4653 (2007)
62. H. Vakilifard, R. Ghasemi, Surf. Coat. Technol. **326**, 470 (2017)
63. Y. Liu, C. Persson, J. Wigren, J. Therm. Spray Technol. **13**, 415 (2004)
64. S. Ahmaniemi, P. Vuoristo, T. Mantyla, C. Gualco, A. Bonadei, R.D. Maggio, Surf. Coat. Technol. **190**, 378 (2005)
65. M.R. Loghman-Estarki, R.S. Razavi, H.M. Edris Pourbafrany, H. Jamali, R. Ghasemi, Ceram. Int. **40**, 1405 (2014)
66. E. Delon, F. Ansart, S. Duluard, J.P. Bonino, D. Monceau, R. Rouaix, A. Thouron, A. Malie, A. Joulia, L. Bianchi, P. Gomez, J. Eur. Ceram. Soc. **38**, 4719 (2018)
67. F. Blas, F. Ansart, P. Lours, J.-P. Bonino, S. Duluard, V. Vidal, L. Pin, G. Pujol, L. Bonin, Surf. Coat. Technol. **334**, 71 (2018)

Publisher's Note Springer Nature remains neutral with regard to jurisdictional claims in published maps and institutional affiliations.